In-plane magnetic anisotropy and magnetization reversal in phase-separated $(La_{0.5}Pr_{0.5})_{0.625}Ca_{0.375}MnO_3$ thin films

Surendra Singh,[1,2,*] J. Olamit,[3,†] M. R. Fitzsimmons,[4,5] J. D. Thompson,[3] H. Jeen,[6] and A. Biswas[7]

[1]*Solid State Physics Division, Bhabha Atomic Research Centre, Mumbai 400085, India*
[2]*Homi Bhabha National Institute, Anushaktinagar, Mumbai 400094, India*
[3]*Los Alamos National Laboratory, Los Alamos, New Mexico 87545, USA*
[4]*Oak Ridge National Laboratory, Oak Ridge, Tennessee 37831, USA*
[5]*Department of Physics and Astronomy, University of Tennessee at Knoxville, Knoxville, Tennessee 37996, USA*
[6]*Department of Physics, Pusan National University, Busan 46241, Republic of Korea*
[7]*Department of Physics, University of Florida, Gainesville, Florida 32611, USA*

(Received 25 July 2022; revised 23 December 2022; accepted 4 January 2023; published 24 January 2023)

The dynamics and interaction of different electronic phases near the metal-to-insulator transition of the phase-separated $(La_{0.5}Pr_{0.5})_{0.625}Ca_{0.375}MnO_3$ (LPCMO) thin film grown on NGO substrate was studied using the first-order reversal curves (FORC) diagram method for electric transport measurements. The in-plane angle-dependent remanence and coercivity field in the region of the ferromagnet metallic phase was measured using the macroscopic magnetization technique. These measurements suggest an in-plane uniaxial magnetic anisotropy for the film with a uniaxial anisotropic constant (Ku) of $\sim 1.2 \times 10^6$ erg/cm^3 at 20 K. The angle dependence of the coercivity is best described by $1/\cos\theta$ dependence indicating that the magnetization reversal occurs mainly through the depinning of the domain wall, a signature of nucleation and propagation mechanism. The correlation of FORC measurements, resistance relaxation, and macroscopic magnetic measurements indicate a fast reversal of electronic and magnetic phases towards the denser phase region and strong interaction of different phases for the LPCMO system.

DOI: 10.1103/PhysRevB.107.024420

I. INTRODUCTION

Complex transition metal oxides with perovskite structures, such as manganites, possess strong electronic correlations and display magnetoelectronic phase separation, which plays a key role in the understanding of some of their most attractive properties like colossal magnetoresistance (CMR), colossal electroresistance (CER), colossal piezoresistance (CPR), and metal-to-insulator transition (MIT) [1–7]. The close competition between various ground states and the interplay of charge, spin, and lattice degrees of freedom leads to the spatial coexistence of multiple phases, even in chemically homogeneous phases [6,8]. Mixed valance bulk $(La_{1-y}Pr_y)_{1-x}Ca_xMnO_3$ (LPCMO) manganites have been studied in the search for magnetoelectronic phase separation in the range of nanometers to microns [9–15]. Thin films of LPCMO systems have shown properties distinct from bulk behavior because of the additional handle (strain driven) available in the case of thin films. Experimental and theoretical studies on manganite films suggested that the strain field can tune the transport and magnetic properties as well as the phase coexistence [9,16–23].

LPCMO is a prototypical electronic phase-separated system which shows the coexistence of different phases on a large length scale of a nanometer (nm) to the micron. LPCMO with $x = 0.33$ and $x = 0.375$ (for $y = 0.6$) are two manganites with slightly different compositions that show a phase separation of nm and micron, respectively, in their bulk phase [9,12]. While LPCMO films with $x = 0.33$ have been investigated extensively for studying different phenomena like magnetic-anisotropy-driven single to multidomain transition [16], coupling of bending strain and magnetism [17–20], electronic phase separation (EPS) [20–23], correlation of electronic and magnetic phases [22,23], and electric field-driven phase separation [2,24], the LPCMO film with $x = 0.375$ has been studied hardly even though a larger phase separation (length $\sim$ micron) was suggested for this system in their bulk [12]. Using x-ray resonant magnetic scattering (XRMS), Singh *et al.* [23] correlated the electronic and magnetic phases across MIT temperature of the LPCMO thin film with $x = 0.375$ and found a larger in-plane charge-magnetic correlation length as compared to that of LPCMO film with $x = 0.33$, indicating larger length scale for phase coexistence in the LPCMO thin film with $x = 0.375$.

The electrical transport (resistance) measurements from these LPCMO films [16,22,23] have also shown different temperature evolution, e.g., changes in MIT and thermal hysteresis. Dhakal *et al.* [2] studied the effect of strain and electric field on transport properties of LPCMO films with $x = 0.33$ and different y (= 0.4, 0.5, and 0.6) and observed that the MIT

*surendra@barc.gov.in
†Present address: United States Patent and Trademark Office, Alexandria, Virginia 22314, USA.

temperature decreases with an increase of Pr concentration, in agreement with the bulk LPCMO [12]. The study also suggested that long-range strain interactions stabilize the ferromagnetic metallic (FMM) phase at low temperatures and a fluid-phase-separated (FPS) state at intermediate temperatures for LPCMO film with $y \geqslant 0.5$, analogous to the strain-liquid phase in bulk LPCMO. A strong dependence of magnetic dynamics on the phase-separated state and morphology of the magnetic domains is also suggested for LPCMO films with $x = 0.50$ [25]. The study also suggested that magnetic dynamics can be a possible route for controlling the phase separation in this system for the realization of device application. The thermal hysteresis behavior of transport and magnetic properties of the LPCMO system further influences the dynamics of different phases and thus impacts the magnetic properties across MIT, which is desirable for the design of future magnetic devices. First-order reversal curve (FORC) analysis is a powerful tool for studying the hysteresis behavior in various systems [26–29]. The FORC diagram and analysis are used extensively for magnetic systems for understanding the phase coexistence, interactions, and dynamics of the magnetic state of the system. Ramirez *et al.* [28] have used this method to analyze the hysteric behavior in transport measurements near the MIT of VO_2 thin films.

Here we report the transport and magnetic properties of a single crystal LPCMO film with $x = 0.375$ and $y = 0.5$ grown on (110) $NdGaO_3$ (NGO) substrate with anisotropic in-plane strain and found an in-plane magnetic anisotropy for the film. X-ray reflectivity (XRR) and polarized neutron reflectivity (PNR) techniques were used to investigate the depth-dependent structure and magnetic depth profile of the film. The electrical transport (resistance) and macroscopic magnetization measurements showed thermal hysteresis of ferromagnetic (metallic) order in the film suggesting a first-order ferromagnetic (metallic) transition. The MIT for LPCMO film was observed at a much lower temperature ($\sim$111 K) than the ferromagnetic transition temperature ($\sim$132 K). The thermal hysteresis for transport data ($\sim$6 K) almost coincides with the thermal hysteresis of magnetization. Taken together the observations suggest percolation of the metallic phase does not occur until after the considerable formation of the magnetic phase. However, like the other LPCMO phase ($x = 0.33$ and $y = 0.6$) [16–23], the anisotropic in-plane epitaxial strain shows isotropic transport properties but significantly different magnetic properties. FORC measurements were performed to study the reversible properties of different electronic phases near the MIT, which show behavior consistent with the relaxation of phase separation near MIT. Further, we study the magnetization reversal mechanism of the LPCMO film by measuring the angular dependence of magnetic properties at low temperatures, suggesting that the magnetization reversal occurs mainly through the depinning of the domain wall.

II. EXPERIMENTAL

A 20-nm-thick LPCMO film with $x = 0.375$ and $y = 0.5$ was epitaxially grown on a (110) NGO single-crystal substrate using pulsed KrF laser (248 nm) deposition [16]. The substrate temperature and O_2 partial pressure were kept at 1053 K and 17.33 Pa, respectively, during the growth of the film. We used a laser fluence of 0.5 J/cm^2, and the repetition rate of the pulsed laser was 5 Hz. The LPCMO film grown on (110) NGO substrate with two perpendicular in-plane directions of $(1\bar{1}0)$ and (001) shows asymmetric strain due to lattice mismatch between NGO substrate and LPCMO film, and the strains along these directions are $\delta_{1\bar{1}0} = 0.49\%$ and $\delta_{001} = 0.26\%$ (an expansion) [16].

XRR measurements in specular (angle of incidence = angle of reflection) and off-specular (angle of incidence $\neq$ angle of reflection) conditions were used to elucidate the depth-dependent layer structure and interface morphology, respectively [30–33]. The inset (lower) of Fig. 1(a) shows the scattering geometry for reflectivity in the reciprocal space. The specular reflectivity $[\theta_i = \theta_f = \theta]$ is measured as a function of the wave-vector transfer component Q_z, normal to the sample surface and is given as $Q_z = \frac{2\pi}{\lambda}[\sin(\theta_i) + \sin(\theta_f)] = \frac{4\pi}{\lambda}\sin\theta$, with λ as the wavelength of the probe (x-ray/neutron) [30–33], while the in-plane wave vector transfer $Q_x = \frac{2\pi}{\lambda}[\cos(\theta_f) - \cos(\theta_i)]$ contributes to the off-specular (diffuse) reflectivity $(\theta_i \neq \theta_f)$ [30–33] for determining the in-plane structure and morphology. The off-specular XRR provides the height-height correlation at different interfaces [33], and for the self-affine fractal surface it is defined as [33] $C(x, y) = \langle \delta z(0)\delta z(x, y)\rangle = \sigma^2 \exp(-[\frac{r}{\xi}]^{2h})$, where σ, h, and ξ are a root-mean-square roughness (a true height-height fluctuation), Hurst parameter, and in-plane height-height correlation length, respectively. The exponent $0 < h < 1$ determines the fractal dimension $(D = 3 - h)$ of the interface (i.e., how jagged the interface is; the larger value of h represents smoother interfaces).

III. RESULTS AND DISCUSSION

Figure 1(a) shows the specular XRR data (symbols) and corresponding fit (solid lines) for LPCMO film. The inset (upper) of Fig. 1(a) shows the electron scattering length density (ESLD) depth profiles obtained from specular XRR data, suggesting an LPCMO film thickness of $\sim$180 Å. Specular XRR results also suggested variation of ESLD profiles near two interfaces (substrate-film and film-air interfaces) and a smaller roughness (<5 Å) at the interfaces. The variation in ESLD near interfaces is due to a small change in composition at interfaces, and it is consistent with other reports on LPCMO films with different compositions grown using similar growth parameters [17–19,23].

Figures 1(b) and 1(c) show the off-specular (diffuse) XRR data (symbols) and fits (solid lines) for the LPCMO film in the detector scan [33,34] around $Q_z = 0.179$ and 0.216 Å^{-1}, respectively. To fit off-specular XRR data, the morphological parameters (σ, h, and ξ) at the interface were varied while keeping the thickness and ESLD parameters, obtained from specular XRR, constant. Analysis of the diffuse XRR data for the film shows similar roughness (σ) values as obtained from specular XRR, suggesting negligible intermixing at interfaces; however, the other morphological parameters obtained from diffuse XRR suggested drastically different morphology for the film as compared to that of the substrate. The other interface morphological parameters obtained from diffuse XRR were $h\,(\xi) = 0.60 \pm 0.08$ (500 ± 50 Å) and

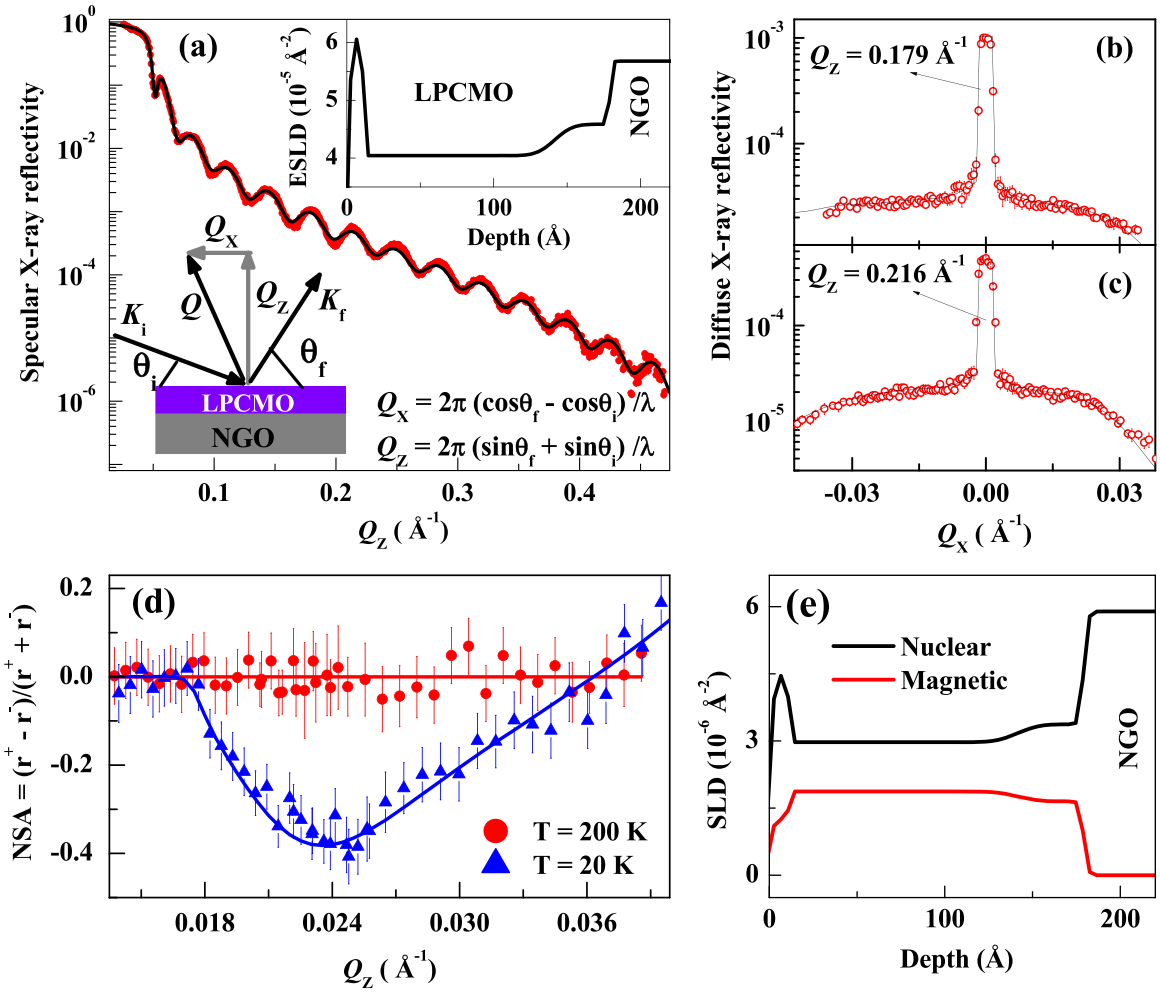

FIG. 1. Specular XRR measurements from LPCMO film. The inset (lower) of (a) shows the reflectivity geometry in reciprocal space. Inset (upper) of (a) shows the electron scattering length density (ESLD) depth profile of the film. Diffuse (off-specular) XRR data (open circles) and corresponding fit (solid lines) from the film at two different angles of incidences with $Q_z = 0.179\,\text{Å}^{-1}$ (b) and $0.216\,\text{Å}^{-1}$ (c). (d) Normalized spin asymmetry (NSA) data (symbols) with the corresponding fit (solid lines) for the film at 200 and 20 K. (e) nuclear and magnetic SLD depth profiles of the sample at 20 K.

0.20 ± 0.03 (5000 ± 500 Å) for substrate-film and film-air (surface) interfaces, respectively. The morphological LPCMO film shows that the film surface is jagged ($h \sim 0.20$) with a fractal dimension (D) close to 3.0, and the height distribution is correlated over a larger lateral length scale (~5000 Å). The in-plane height-height correlation length for this film is on the lower side of the range for charge-charge correlation length (~9000 Å) obtained for LPCMO films grown under similar conditions [23]. However, it matches the in-plane charge-magnetic correlation length measured by the resonant x-ray magnetic scattering technique [23], indicating a similar length scale for structure and magnetic interface roughness for the LPCMO film in the present case.

The depth-dependent magnetization averaged over the lateral size (~$1.0\,\text{cm}^2$) of the film at a temperature across MIT was investigated with specular PNR measurements. Specular PNR data were measured by applying an in-plane magnetic field of ~2 kOe along the easy direction of the film. The difference between spin-dependent reflectivity ($r^{\pm}$), where the $\pm$ sign indicates the parallel (antiparallel) alignment of neutron spin with the applied magnetic field (H), providing detailed depth-dependent magnetization or magnetic scattering length density (MSLD). Figure 1(d) shows the normalized spin asymmetry (NSA) data (symbols), defined as NSA $= (r^+ - r^-)/(r^+ + r^-)$, and corresponding fits (solid lines) for the film at 200 (well above the curie temperature of the film) and 20 K. The nuclear scattering length density (NSLD) and MSLD depth profiles of the LPCMO film are shown in Fig. 1(e). The NSLD profiles obtained from PNR measurements are in agreement with the ESLD profile obtained from XRR. PNR results at 20 K show a reduction in magnetization at interfaces, which may be due to a change in chemical structure at interfaces as shown in ESLD and NSLD depth profiles. Using MSLD and NSLD (in Å^{-2}) from PNR, one can obtain the magnetization of the magnetic layer in different units [32]. From PNR data we find a thickness averaged magnetization of $\sim 580 \pm 60\,\text{emu/cm}^3$ ($3.70 \pm 0.40\ \mu_B$/Mn) for the LPCMO film at 20 K.

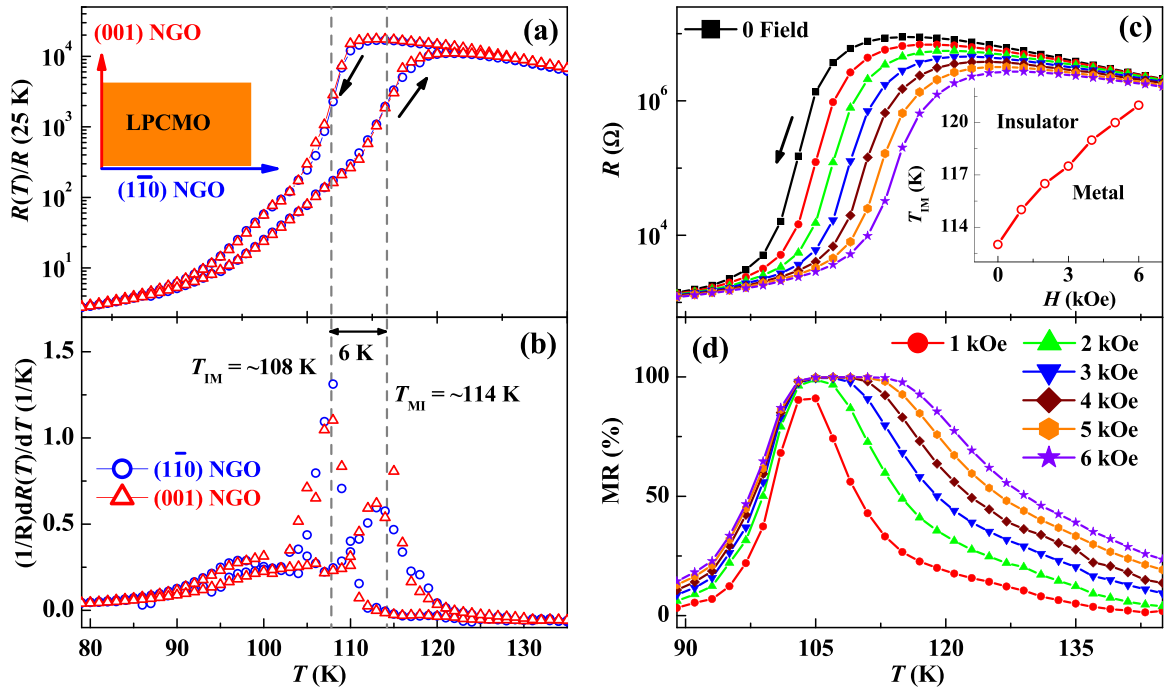

FIG. 2. (a) Resistance ratio as a function of temperature [$R(T)/R$ (25 K)] for the film along two perpendicular in-plane directions. The inset shows the two perpendicular in-plane directions [(001) and (1$\bar{1}$0)] of NGO substrates on which LPCMO film is grown. (b) The $(1/R)\,dR/dT$ curves for resistance data suggest different metal-to-insulator (T_{MI} = ~114 K) and insulator-to-metal (T_{IM} = ~108 K) transition temperatures. (c) Resistance vs temperature during the cooling cycle at different applied magnetic fields. A magnetic field is applied along (1$\bar{1}$0)] of NGO and resistance are also measured along the same directions. Inset shows the variation of T_{MI} as a function of the applied field. (d) MR (%) value at different fields for the cooling cycle.

Figure 2(a) shows the temperature dependence of resistance ratio [$R(T)/R$ (25 K)] along two perpendicular in-plane directions [(1$\bar{1}$0) and (001) NGO directions as shown in the inset of Fig 2(a)] upon cooling and warming the film. The $(1/R)dR/dT$ curves [Fig. 2(b)] show two peaks along the cooling and warming cycles, and the peak temperature corresponds to the insulator-to-metal ($T_{IM} \sim 108$ K, in the cooling cycle) and metal-to-insulator ($T_{MI} \sim 114$ K, in warming cycle) transitions, respectively. The $R(T)$ curves for the film along two perpendicular in-plane directions show a similar value of thermal hysteresis of ~6 K. The average value of the T_{IM} and T_{MI} ($T_{MIT} \sim 111$ K) for the LPCMO film studied here is larger as compared to that of the LPCMO film of similar thickness ($T_{MIT} \sim 76$ K) [16] with slightly different composition studied earlier. However, a large variation in MIT with the thickness of LPCMO films is observed earlier [16–21], which is related to strain-dependent phase separation in this system, and the T_{MIT} generally increases with a decrease in thickness. It is noted that despite asymmetric strain along two perpendicular in-plane directions, we did not observe any significant anisotropy in transport properties. This observation is consistent with an earlier report on LPCMO film with $x = 0.33$ [16,17], but it is in contrast to another study [35], which suggested a large difference in T_{IM} and peak resistivity along two perpendicular in-plane directions of $(La_{0.52}Pr_{0.48})_{1-x}Ca_xMnO_3$ thin film with $x = 0.375$ grown on NGO substrate due to anisotropic strain. However, such anisotropic strain-dependent transport properties may be plausible if the length scale associated with transport measurements is similar to the phase separation in these systems. The $R(T)$ along the (1$\bar{1}$0) NGO direction in the cooling cycle near T_{IM} at different applied magnetic fields for a similarly grown LPCMO film is shown in Fig. 2(c), suggesting an increase in the T_{IM} on increasing the applied field. We have also estimated the magnetoresistance (MR) [MR(%) = 100×[$R(0)$-$R(H)$]/$R(H)$] at the different applied fields, which is shown in Fig. 2(d) for the cooling cycle around T_{IM}.

FORC measurements for the film on the warming cycle (on increasing the temperature), shown in Fig. 3(a), were obtained as follows [28]: Starting at a temperature of 136 K, where the film is mostly insulating, the sample was cooled to a specific reversal temperature, T_R. On reaching T_R, the sample is warmed to an insulating state (136 K). Thus the path followed by the resistance starting at T_R and ending at 136 K [$R(T_R, T)$] is termed a FORC. The FORC distribution [Fig. 3(b)] is calculated using the mixed second-order derivatives defined as [28] $\rho(T_R, T) = -\partial^2 R(T_R, T)/2\partial T_R \partial T$, and we have used FORCinel software [29] to calculate the FORC distribution as shown in Fig. 3(b). The mixed second-order derivative eliminates a constant resistance under a change in T or T_R, and thus, any nonzero value in the FORC distribution corresponds to irreversible parts in the hysteresis loop [28]. The FORC distribution shows two high-intensity (larger resistance) regions (bright spots) spread in the temperature range with maximum intensity central regions at a (T_R, T) of (120 K, 124 K) and

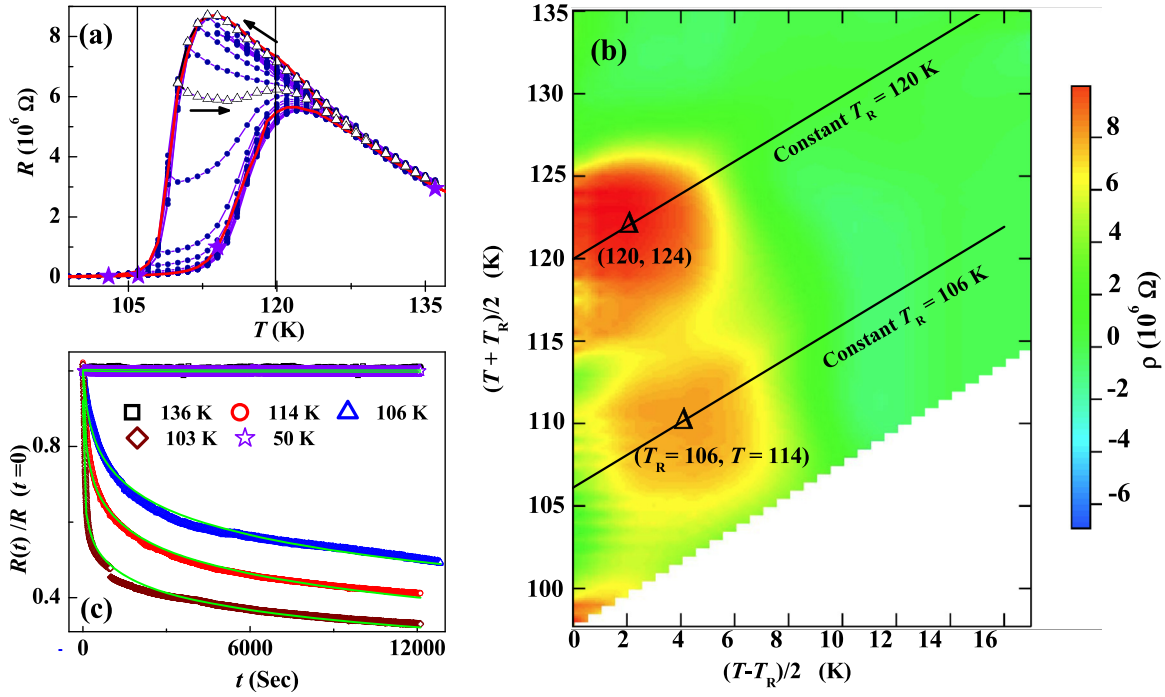

FIG. 3. (a) First-order reversal curves $[R(T_R, T)]$ for LPCMO film. The closed star (violet) points on the $R(T)$ curve during the warming cycle are the temperatures at which we measured the resistance relaxation. T_R is the reversal temperature, and temperature direction is changed for FORC measurements (see text). (b) The corresponding contour plot distribution (2D FORC diagram). (c) Relative variation of resistance of LPCMO film as a function of time for different temperatures.

(106 K, 114 K), shown as two open triangles in Fig. 3(b). The two solid (black) lines in Fig. 3(b) correspond to a constant temperature T_R of 120 and 106 K, which are very near the $T_{\rm MI}$ and $T_{\rm IM}$, respectively, of the film. This suggests that the maximum irreversibility occurs near the $T_{\rm MI}$ and $T_{\rm IM}$ transition temperatures with a higher amount of irreversibility near $T_R =$ 120 K ($\sim T_{\rm MI}$), suggesting a drop in FMM and growth of the reverse domains (insulating phase) at this temperature. While below 106 K the FMM phase grows rapidly and culminates in the irreversible switching of phases. The irreversible behavior of the hysteresis also indicates the dynamic behavior of different phases in the system. The irreversible behavior of the $R(T)$ measurements is also evident in Fig. 3(a), where we have plotted a complete cycle of the $R(T)$ measurements from T_R ($\sim$110 K) to 136 K and back to T_R (open triangle), suggesting that such irreversibility is found much above the $T_{\rm MI}$. The LPCMO film is insulating and fully reversible for temperatures above 136 K, and below it a nonzero part increases as T_R is decreased. The nonzero part of the FORC distributions well above $T_{\rm MI}$ and below $T_{\rm IM}$ suggests significant irreversibility in the variation of resistance with temperature beyond $T_{\rm MIT}$ ($\sim$111 K). This indicates that for the phase coexistence of the FMM and insulating phases above $T_{\rm MIT}$, which acts as a seed for the transition, and well below $T_{\rm MIT}$ the major phase is the FMM. Magnetization measurements discussed later suggest a higher value of magnetic transition temperature ($T_C \sim 132$ K) than the $T_{\rm MIT}$ for this system and thus confirm that the metallic (ferromagnetic) and insulating (nonferromagnetic) phases exist well above the $T_{\rm MIT}$. Therefore, significant irreversibility in FORC measurements well above (near T_C) and below the $T_{\rm MIT}$ ($\sim$111 K) indicates the existence of electronic phase separation (EPS) in this film, and the dynamics of the different phases beyond the $T_{\rm MIT}$ ($\sim$111 K) initiate the transition to the high-phase region from the low-phase region.

The phase coexistence is also manifested in the dynamic behavior of the electric transport measurements, which exhibits that this dependence is closely correlated with the static signatures of the EPS. To gain further insight into the coexistence and phase competition, we have also measured the relaxation of $R(t)$ (resistance as a function of time) at different temperatures across $T_{\rm MIT}$ of LPCMO film, and the results are shown in Fig. 3(c). We found a constant variation for the $R(t)/R(t=0)$ ratio with t (up to $\sim 10^4$ s) for $T = 50$ and 136 K, suggesting the full percolation path of the metallic phase at 50 K and a majority of insulating phases at 136 K. For other temperatures (103, 106, and 114 K) in the range of the thermal hysteresis of the film, we observed that $R(t)/R(t=0)$ is always less than 1. To discuss quantitatively the changes in the relaxation of the $R(t)$ data, we have fitted [solid green lines in Fig. 3(c)] the temporal evolution of the resistance to a phenomenological model given as [36] $R(T,t) = R(t=0) + S_R(T)\ln(\frac{t}{\tau}+1)$, where $R(t=0) = 1$ is the initial normalized resistance, τ is the temperature-dependent relaxation time, and S_R is the resistance relaxation rate (viscosity). The parameter S_R characterizes the dynamic behavior of the phase separation, where the competing phases change their volume fraction as a function of time in a given T range. In this scenario, the $S_R > 0$ behavior is related to the increase of the volume fraction of the insulating phase as a function of time. On the other hand, $S_R < 0$ reflects the metallic phase fraction

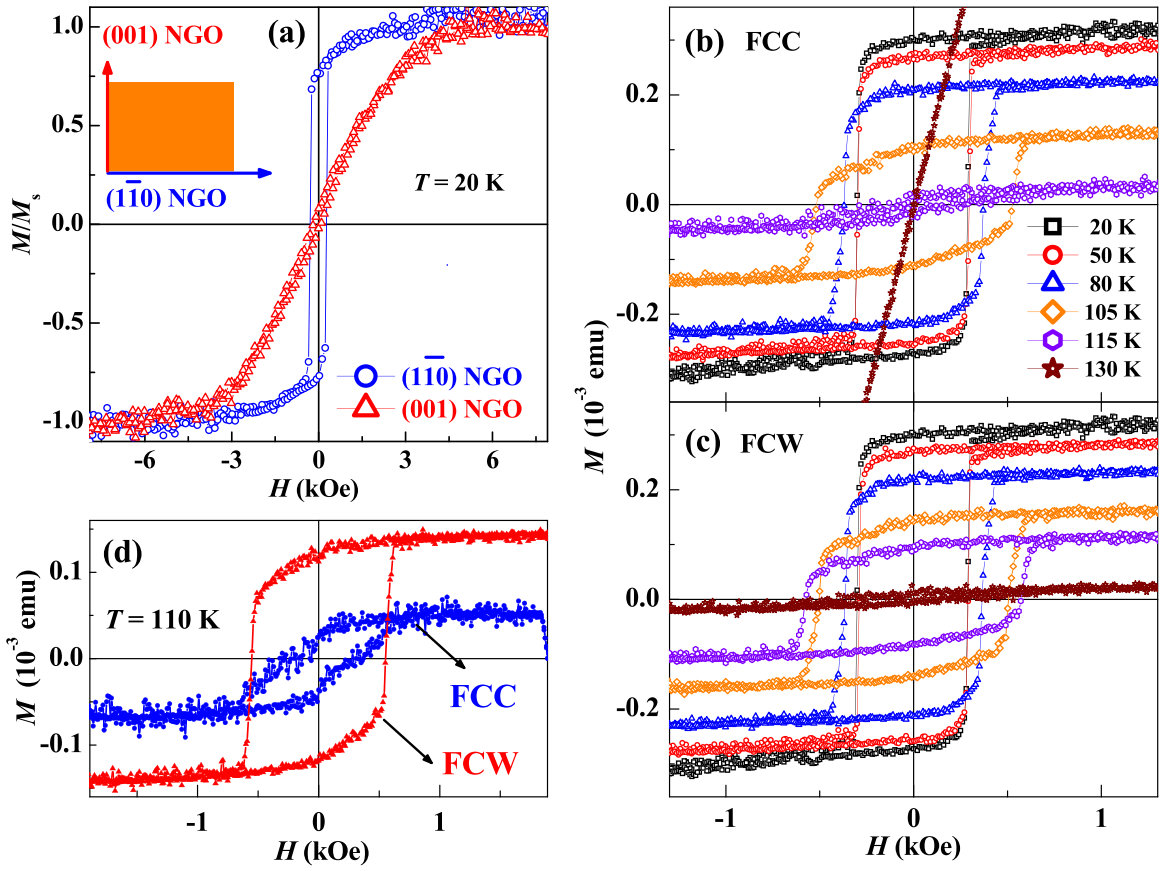

FIG. 4. (a) Hysteresis loops [$M(H)$ curve] for the LPCMO film at 20 K measured by applying an in-plane magnetic field (H) along the (001) and (1$\bar{1}$0) NGO directions, suggesting (1$\bar{1}$0) NGO is an easy axis. $M(H)$ curves along the in-plane easy axis at different temperatures upon (b) field-cooled cooling (FCC) and (c) field-cooled warming (FCW) cycles. (d) Comparison of hysteresis loop at 110 K in FCC and FCW cycle.

growth as a function of time. The parameter S_R is nearly zero at both temperatures 136 and 50 K, where insulating (paramagnetic) and metallic (ferromagnetic) are the dominating state. We found $S_R = -0.065$, -0.1, and $-0.09\,\Omega$ and the corresponding $\tau = 0.5$, 86, and 16 s, from the fit to resistance curves at different temperatures of 114, 106, and 103 K (in the irreversible temperature range), respectively. The negative SR for these temperatures indicate that the resistance relaxation favors the metallic phase in the system at the expense of the insulating phase; however, the relaxation time for such transition is different at different temperatures. The relaxation time for the LPCMO film observed here is shorter than the other manganite film [36] suggesting faster dynamics for the EPS.

In contrast to transport [$R(T)$] measurements, the $M(H)$ data [Fig. 4(a)] exhibit in-plane magnetic anisotropy with (1$\bar{1}$0) and (001) NGO directions as an easy and hard axis, respectively. Figure 4(a) shows the magnetization [$M(H)$] measurements at 20 K (where the major phase is ferromagnetic) for the LPCMO film along two perpendicular in-plane directions. The $M(H)$ measurements were carried out using a superconducting quantum interference device (SQUID) with the vibrating sample magnetometer (VSM), where the field was applied along the plane of the film. The field-cooled (FC) data were taken during the cooling and warming of the sample in a fixed applied field of 500 Oe. To separate the enormous paramagnetic contribution from the substrate, we have subtracted the magnetization data for the identical NGO substrate from the signal of film grown on NGO. The $M(H)$ loop obtained with the applied field parallel to the (1$\bar{1}$0) NGO direction is almost square shaped, indicating that this is the easy axis, while the loop obtained with the field parallel to the (001) NGO direction shows an almost linear dependence of the magnetization on the applied field (the magnetic hard axis direction). This suggests a uniaxial behavior for LPCMO film, and it is consistent with earlier measurements on LPCMO films with $x = 0.33$ [16–23]. It is evident from Fig. 4(a) that the LPCMO film at 20 K shows an anisotropic field (H_a) of ∼4 kOe. We have estimated the uniaxial anisotropic constant (K_u) of $\sim 1.2 \times 10^6$ erg/cm^3 for the film at 20 K using thickness-averaged magnetization (∼ saturation magnetization, M_s) of the film (∼580 emu/cm^3) obtained from PNR, H_a (∼4 kOe), and the relation $K_u = M_s H_a/2$. This value of K_u is comparable to that of LPCMO film ($\sim 1.0 \times 10^6$ erg/cm^3) with $x = 0.33$ [16] and $La_{0.7}Ca_{0.3}MnO_3$ thin films (3.6×10^5 erg/cm^3 at 77 K) on NGO substrates [37]. We have also carried out $M(H)$ measurements at different temperatures along an easy axis [(1$\bar{1}$0) NGO] upon field-cooled cooling (FCC) and field-cooled warming (FCW) cycles as shown in Figs. 4(b) and 4(c), respectively. A comparison of the $M(H)$

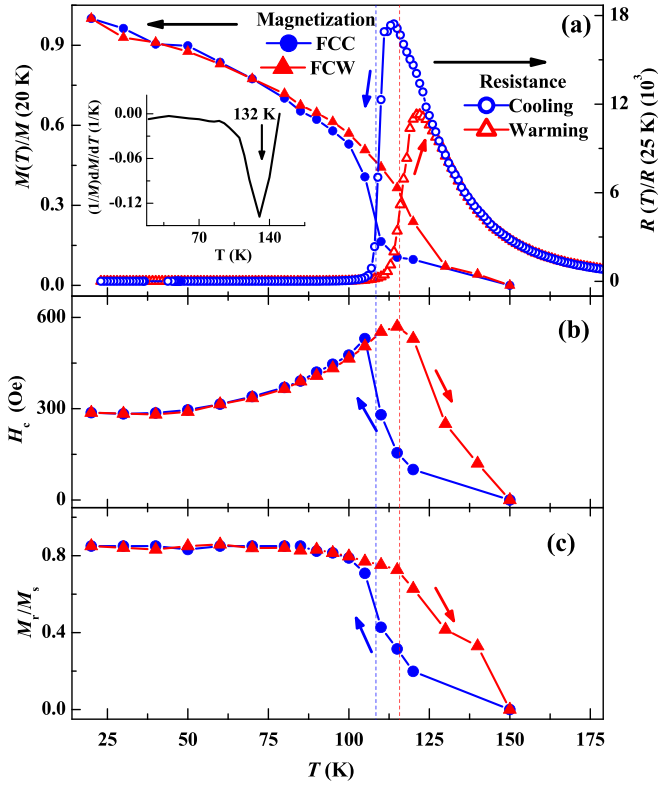

FIG. 5. Temperature-dependent variation of (a) magnetization ratio $[M(T)/M(20\,\mathrm{K})]$, (b) coercive field (H_c), and (c) ratio of remanent magnetization and saturation magnetization $[M_r/M_s]$ along the easy axis ([1$\bar{1}$0] NGO direction), upon field-cooled cooling (FCC) and field-cooled warming (FCW) cycles. The transport measurements upon cooling and warming are also plotted in (a). The inset of (a) shows the temperature variation of $(1/M)dM/dT$ data suggesting a transition temperature of ∼132 K.

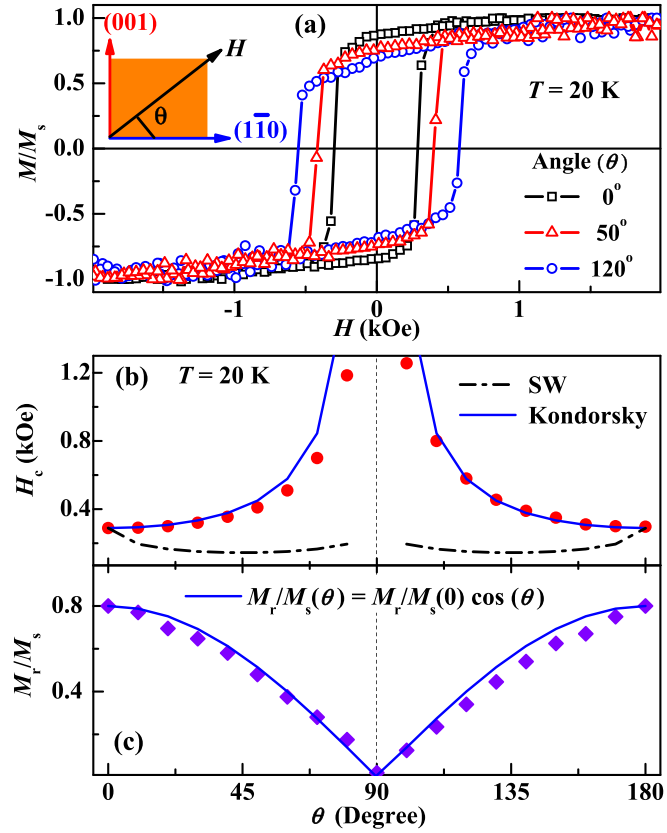

FIG. 6. (a) Reduced $M(H)$ curves at 20 K along different angles from the in-plane easy axis. The inset shows the direction of the angle at which the field was applied. Variation of (b) H_c and (c) M_r/M_s, at 20 K with the in-plane angle of applied filed with respect to the easy axis.

curve at 110 K measured along the easy axis for FCC and FCW is shown in Fig. 4(d), suggesting a higher volume fraction of the FM phase in the FCW cycle.

The temperature dependence of the normalized magnetization $[M(T)/M\ (20\ \mathrm{K})]$, coercive field ($H_c$) and the ratio ($M_r/M_s$) between remanent magnetization (M_r) and saturation magnetization (M_s) along the easy axis obtained from $M(H)$ measurements under FCC and FCW cycles are shown in Figs. 5(a), 5(b), and 5(c), respectively. The $M(T)$ data at limited temperature values during FCC and FCW cycles, shown in Fig. 5(a), are the saturation magnetization obtained from the $M(H)$ curves shown in Fig. 4. The paramagnetic to ferromagnetic transition (Curie temperature, T_C) for these phase-separated systems is usually a temperature with nonzero magnetization. However, we have also plotted the temperature variation of $(1/M)\ dM/dT$ in the inset of Fig. 5(a) and estimated the T_C of ∼132 K for this system, which is again the temperature where we observed nonzero magnetization. A clear thermal hysteresis in these properties is evident from Fig. 5, which almost coincides with the thermal hysteresis observed in transport measurements and thus describes a first-order transition in the system. However, the MIT temperature is lower than the observed T_C for the LPCMO film.

Experimentally the magnetization reversal mechanism is usually inferred from the angular dependence of coercivity. Thus, the angle-dependent $M(H)$ measurements, with the field applied in the plane of the film, were performed at $T = 20$ K, where the majority phase is ferromagnetic and will help a better understanding of the magnetization reversal in this system. The in-plane angle (θ) of the applied field with the easy axis [(1$\bar{1}$0) NGO direction], shown in the inset of Fig. 6(a), was varied to determine the magnetic anisotropy. For all field angles, a full $M(H)$ loop was measured for the estimation of H_c and M_r, as a function of θ. Figure 6(a) shows the $M(H)$ curves at 20 K for the film with the field-aligned at different θ of 0°, 50°, and 120°. Figures 6(b) and 6(c) show the in-plane angular dependence of the H_c and remanence ratio (M_r/M_s), respectively.

In general, the magnetic field-driven magnetization reversal in ferromagnetic systems with uniaxial anisotropy can be approximated either by the Stoner-Wohlfarth (SW) model, which is based on the coherent rotation of magnetic moments in very small particles [38,39], or the Kondorsky model [40,41], which treats reversal using a model of domain nucleation and domain wall motion. The SW model describes magnetic switching behavior for single domain particles and switching phenomena are related as [42] $H_c(\theta) = H_c(0)(\cos^{2/3}\theta + \sin^{2/3}\theta)^{-3/2}$, while in the case of the

Kondorsky model, the magnetic switching processes involve the nucleation of multidomain structures and displacement of domain walls plays an important role in producing such multidomain structures. Thus, for a uniaxial magnetic system in which the reversal mechanism is controlled by domain wall depinning, the coercivity is in its simplest form described by the Kondorsky relation [40,41]: $H_c(\theta) = H_c\ (0)/\cos\theta$. We have fitted the $H_c\ (\theta)$ curve for LPCMO film at 20 K, shown in Fig. 6(b), using these models. The black dash-dot line is the profile for the SW model, which does not follow the observed variation of the H_c, whereas the data were well fitted with the Kondorsky model, which is consistent with earlier reports on manganite films [16,43]. However, it is in contrast with the studies on LSMO films grown on STO and NGO substrates, which suggested a two-phase model (both coherent rotation and domain wall motion) for explaining the switching behavior of the magnetization [44,45]. The drastically different angular variations of coercivity for LSMO [44] and LPCMO film suggest that the strong phase separation in LPCMO film contributes to the Kondorsky rule for the nucleation and growth of the magnetic domain as compared to the two-phase model described for LSMO film [44]. The angular variation of the experimental remanent magnetization ratio (M_r/M_s) of the LPCMO film [Fig. 6(c)] shows a predominantly uniaxial anisotropy dependence with $M_r/M_s(\theta) = M_r/M_s(0)|\cos\theta|$, due to the projection of the easy axis magnetization onto the axis of observation. This dependency is plotted with the solid blue line in Fig. 6(c).

The LPCMO system with $x = 0.375$ and $y = 0.6$ shows the electronic domain of metallic and insulating phases in the size of a few microns for both bulk [12] and thin film [23] systems, which is much larger than the domain size (∼nm) shown by other LPCMO films with $x = 0.33$ [21,23]. The corresponding magnetic responses of the LPCMO system for these electronic phases are the ferromagnetic (metallic), antiferromagnetic charge order (insulating) and paramagnetic (insulating) phases [9,12,13], and the coexistence of these phases is responsible for the CMR and MIT properties. The diffuse XRMS study also suggested the one-to-one correspondence for charge-charge (electronic) and charge-magnetic (magnetic) correlation length (∼domain size) for LPCMO films with a larger correlation length for the LPCMO film with $x = 0.375$ phase [22,23]. The coexistence of larger length scales of different phases in the LPCMO film with $x = 0.375$ was also attributed to the smaller thermal hysteresis and higher TMIT for this phase [23]. Usually, the fast reversal of magnetization is related to the magnetic domain size, and for large magnetic domains, the reversal is faster. Like other manganite films [16,43], this system also shows a Kondorsky model $(1/\cos\theta)$ for magnetization reversal and leads to a single to multidomain transition. However, we believe that the larger length scale for the ferromagnetic (metallic) phase will provide a faster reversal for this system. A relatively shorter relaxation time for this system also suggests the fast dynamic of the phases across MIT.

IV. SUMMARY

In summary, a clear thermal hysteresis was observed in the transport and macroscopic magnetic properties of LPCMO film grown on NGO substrate, suggesting a first-order transition and indication of phase separation in the system. FORC measurements provided dynamics of different phases near T_{MIT} and suggested the coexistence of interacting metallic (ferromagnetic) and insulating phases well above and below the T_{MIT}. The relaxation of electrical transport properties suggested a fast relaxation towards the dense phase (conducting phase below MIT and insulating phase above MIT). The angular dependence of the remanence and coercivity of the LPCMO film grown on NGO substrate shows in-plane uniaxial magnetic anisotropy, which may be due to the presence of in-plane anisotropic strain. The angle dependence of the coercivity is best described by a Kondorsky model, suggesting magnetization reversal starts with the depinning of domain walls (nucleation and growth of a larger magnetic domain). This behavior as compared to SW, shown by LPCMO film, may provide an opportunity for possible application in magnetic device structures.

[1] S. Jin, T. H. Tiefel, M. McCormack, R. A. Fastnacht, R. Ramesh, and L. H. Chen, Science **264**, 413 (1994).

[2] T. Dhakal, J. Tosado, and A. Biswas, Phys. Rev. B **75**, 092404 (2007).

[3] K. Miyano, T. Tanaka, Y. Tomioka, and Y. Tokura, Phys. Rev. Lett. **78**, 4257 (1997).

[4] A. Asamitsu, Y. Tomioka, H. Kuwahara, and Y. Tokura, Nature (London) **388**, 50 (1997).

[5] J. Tosado, T. Dhakal, and A. Biswas, J. Phys.: Condens. Matter **21**, 192203 (2009).

[6] E. Dagotto, T. Hotta, and A. Moreo, Phys. Rep. **344**, 1 (2001).

[7] M. Fath, S. Freisem, A. A. Menovsky, Y. Tomioka, J. Aarts, and J. A. Mydosh, Science **285**, 1540 (1999).

[8] Y. Tokura and Y. Tomioka, J. Magn. Magn. Mater. **200**, 1 (1999).

[9] K. H. Ahn, T. Lookman, and A. R. Bishop, Nature (London) **428**, 401 (2004).

[10] M. B. Salamon and M. Jaime, Rev. Mod. Phys. **73**, 583 (2001).

[11] T. Becker, C. Streng, Y. Luo, V. Moshnyaga, B. Damaschke, N. Shannon, and K. Samwer, Phys. Rev. Lett. **89**, 237203 (2002).

[12] M. Uehara, S. Mori, C. H. Chen, and S.-W. Cheong, Nature (London) **399**, 560 (1999).

[13] L. Zhang, C. Israel, A. Biswas, R. L. Greene, and A. Lozanne, Science **298**, 805 (2002).

[14] L. Ghivelder and F. Parisi, Phys. Rev. B **71**, 184425 (2005).

[15] D. D. Sarma, D. Topwal, U. Manju, S. R. Krishnakumar, M. Bertolo, S. La Rosa, G. Cautero, T. Y. Koo, P. A. Sharma, S.-W. Cheong, and A. Fujimori, Phys. Rev. Lett. **93**, 097202 (2004).

[16] H. Jeen and A. Biswas, Phys. Rev. B **83**, 064408 (2011).

[17] S. Singh, M. R. Fitzsimmons, T. Lookman, J. D. Thompson, H. Jeen, A. Biswas, M. A. Roldan, and M. Varela, Phys. Rev. Lett. **108**, 077207 (2012).

[18] S. Singh, M. R. Fitzsimmons, T. Lookman, H. Jeen, A. Biswas, M. A. Roldan, and M. Varela, Phys. Rev. B **85**, 214440 (2012).

[19] S. Singh, M. R. Fitzsimmons, T. Lookman, H. Jeen, and A. Biswas, Phys. Rev. B **90**, 060407(R) (2014).

[20] S. Singh, M. R. Fitzsimmons, H. Jeen, and A. Biswas, Appl. Phys. Lett. **104**, 201602 (2014).
[21] S. Singh, M. R. Fitzsimmons, H. Jeen, A. Biswas, and M. E. Hawley, Appl. Phys. Lett. **101**, 022404 (2012).
[22] S. Singh, J. W. Freeland, M. R. Fitzsimmons, H. Jeen, and A. Biswas, J. Appl. Phys. **116**, 222205 (2014).
[23] S. Singh, J. W. Freeland, M. R. Fitzsimmons, H. Jeen, and A. Biswas, Sci. Rep. **6**, 29632 (2016).
[24] H. Jeen and A. Biswas, Phys. Rev. B **88**, 024415 (2013).
[25] D. Carranza-Celis, E. Skoropata, A. Biswas, M. R. Fitzsimmons, I. K. Schuller, and J. G. Ramirez, Phys. Rev. Mater. **5**, 124413 (2021).
[26] C. R. Pike, A. P. Roberts, and K. L. Verosub, J. Appl. Phys. **85**, 6660 (1999).
[27] R. K. Dumas, C. P. Li, I. V. Roshchin, I. K. Schuller, and K. Liu, Phys. Rev. B **75**, 134405 (2007).
[28] J.-G. Ramírez, A. Sharoni, Y. Dubi, M. E. Gómez, and Ivan K. Schuller, Phys. Rev. B **79**, 235110 (2009).
[29] R. J. Harrison and J. M. Feinberg, Geochem. Geophys. Geosyst. **9**, Q05016 (2008).
[30] L. G. Parratt, Phys. Rev. **95**, 359 (1954).
[31] S. Singh, M. Swain, and S. Basu, Prog. Mater. Sci. **96**, 1 (2018).
[32] M. R. Fitzsimmons and C. Majkrzak, *Modern Techniques for Characterizing Magnetic Materials* (Springer, New York, 2005), p. 107.
[33] S. K. Sinha, E. B. Sirota, S. Garoff, and H. B. Stanley, Phys. Rev. B **38**, 2297 (1988).
[34] J. P. Schlomka, M. Tolan, L. Schwalowsky, O. H. Seeck, J. Stettner, and W. Press, Phys. Rev. B **51**, 2311 (1995).
[35] T. Z. Ward, J. D. Budai, Z. Gai, J. Z. Tischler, L. Yin, and J. Shen, Nat. Phys. **5**, 885 (2009).
[36] L. Hu, L. Q. Yu, P. Xiong, X. L. Wang, J. H. Zhao, L. F. Wang, Z. Huang, and W. B. Wu, Phys. Rev. B **97**, 214428 (2018).
[37] N. D. Mathur, M. H. Jo, J. E. Evetts, and M. G. Blamire, J. Appl. Phys. **89**, 3388 (2001).
[38] E. C. Stoner and E. P. Wohlfarth, Philos. Trans. R. Soc. Lond. A **240**, 599 (1948).
[39] C. Tannous and J. Gieraltowski, Eur. J. Phys. **29**, 475 (2008).
[40] D. Givord, P. Tenaud, and T. Viadieu, J. Magn. Magn. Mater. **72**, 247 (1988).
[41] E. Kondorsky, J. Phys. (Moscow) **2**, 161 (1940).
[42] M. Delalande, J. de Vries, L. Abelmann, and J. C. Lodder, J. Magn. Magn. Mater. **324**, 1277 (2012).
[43] Z.-H. Wang, G. Cristiani, and H.-U. Habermeier, Appl. Phys. Lett. **82**, 3731 (2003).
[44] M. Mathews, E. P. Houwman, H. Boschker, G. Rijnders, and D. H. A. Blank, J. Appl. Phys. **107**, 013904 (2010).
[45] H. Boschker, J. Kautz, E. P. Houwman, G. Koster, D. H. A. Blank, and G. Rijnders, J. Appl. Phys. **108**, 103906 (2010).